Supplementary Materials

Tetraruthenium Macrocycles With Laterally Extended Bis(alkenyl) Ligands and Their $F_4TCNQ^{\bullet-}$ Salts

Rajorshi Das [1,*], Michael Linseis [1], Laura Senft [2], Ivana Ivanović-Burmazović [2] and Rainer F. Winter [1,*]

Table of Contents

List of Figures

List of Tables

NMR Spectroscopy

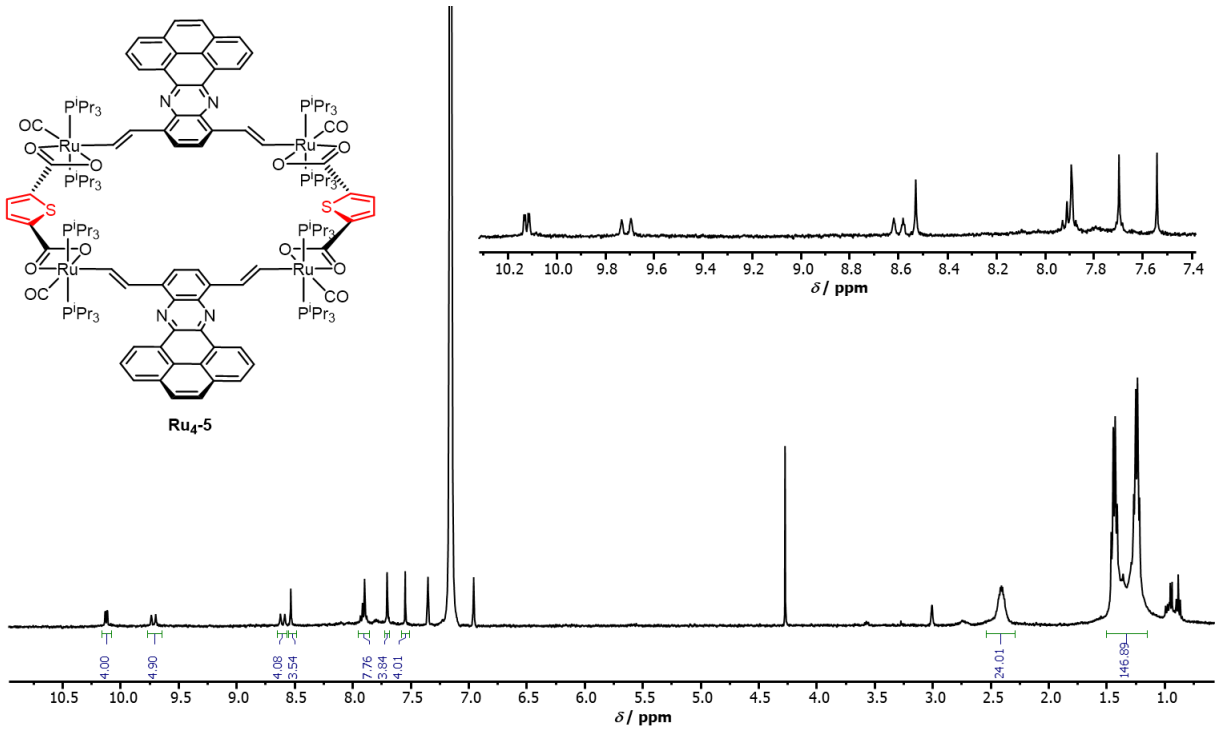

Figure S1. ^{1}H NMR spectrum of **Ru_4-5** measured in C_6D_6 (298 K).

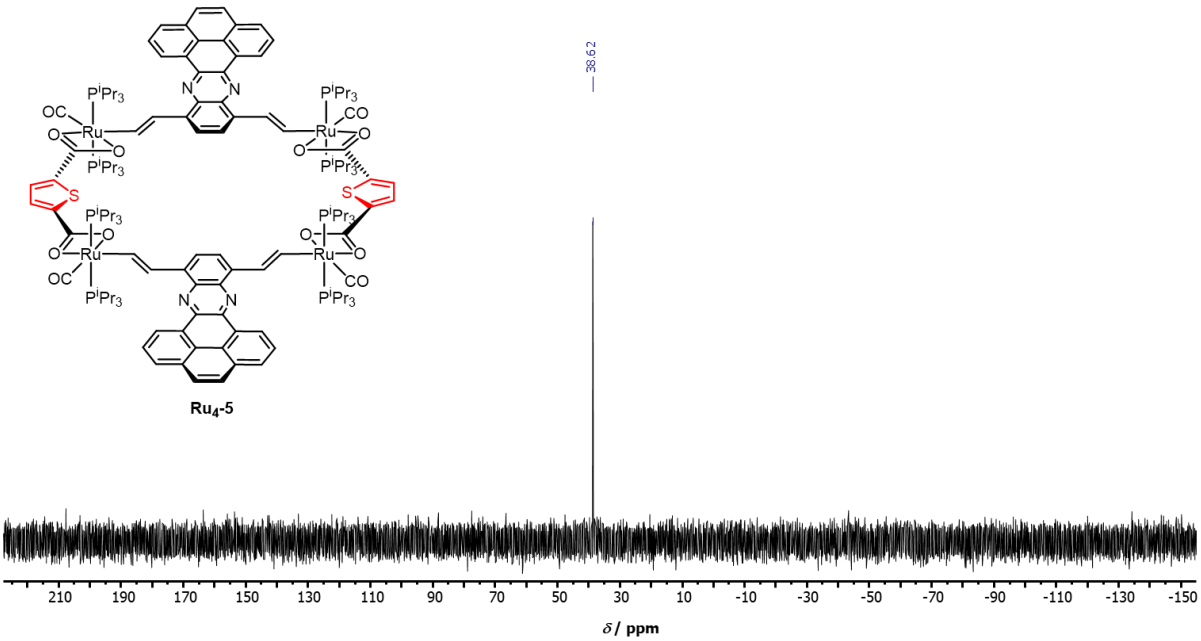

Figure S2. ^{31}P{^{1}H} NMR spectrum of **Ru_4-5** measured in C_6D_6 (298 K).

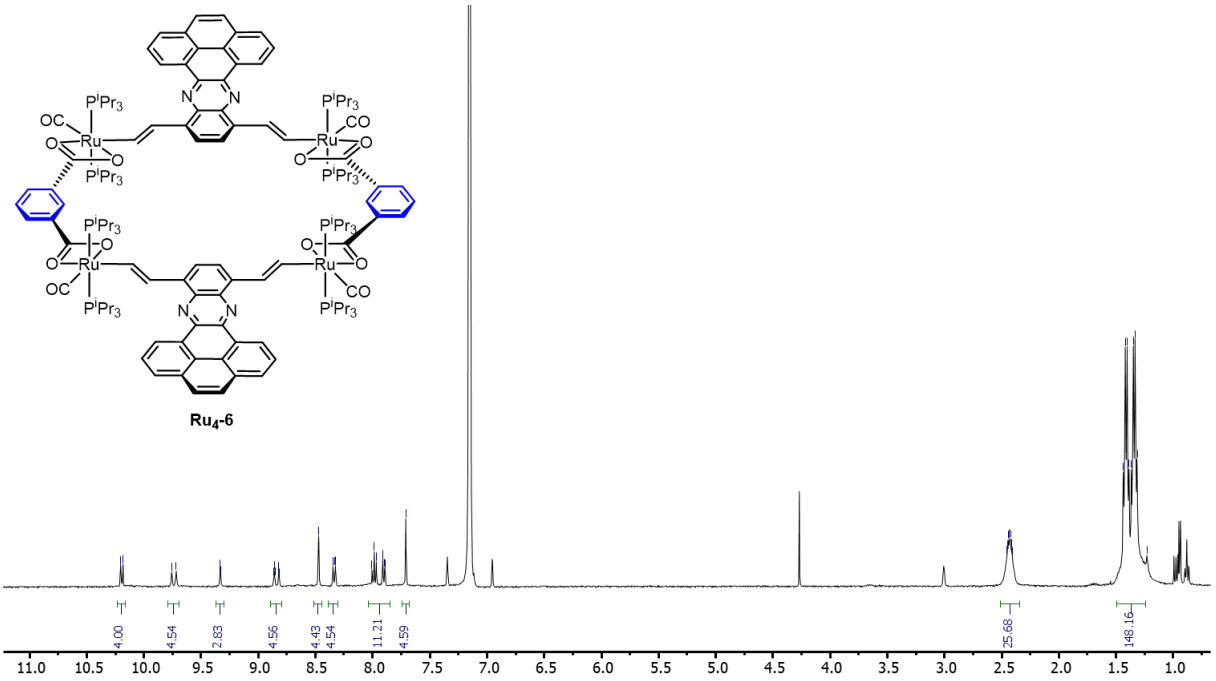

Figure S3. ^{1}H NMR spectrum of **Ru$_4$-6** measured in C_6D_6 (298 K).

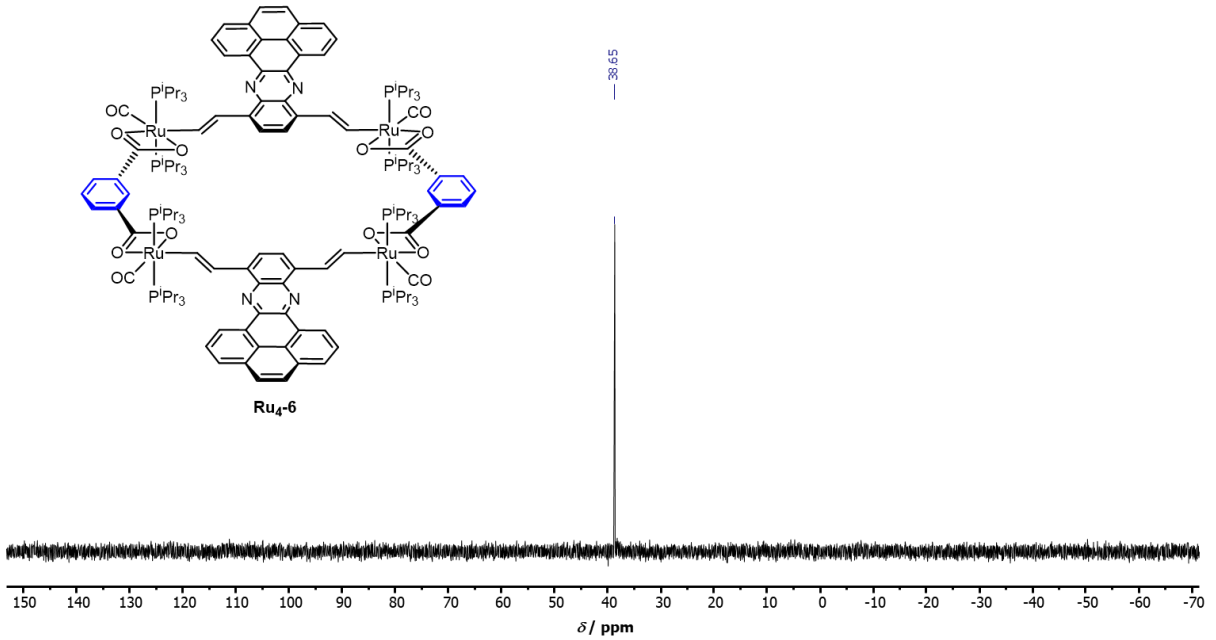

Figure S4. ^{31}P{^{1}H} NMR spectrum of **Ru$_4$-6** measured in C_6D_6 (298 K).

Mass Spectrometry

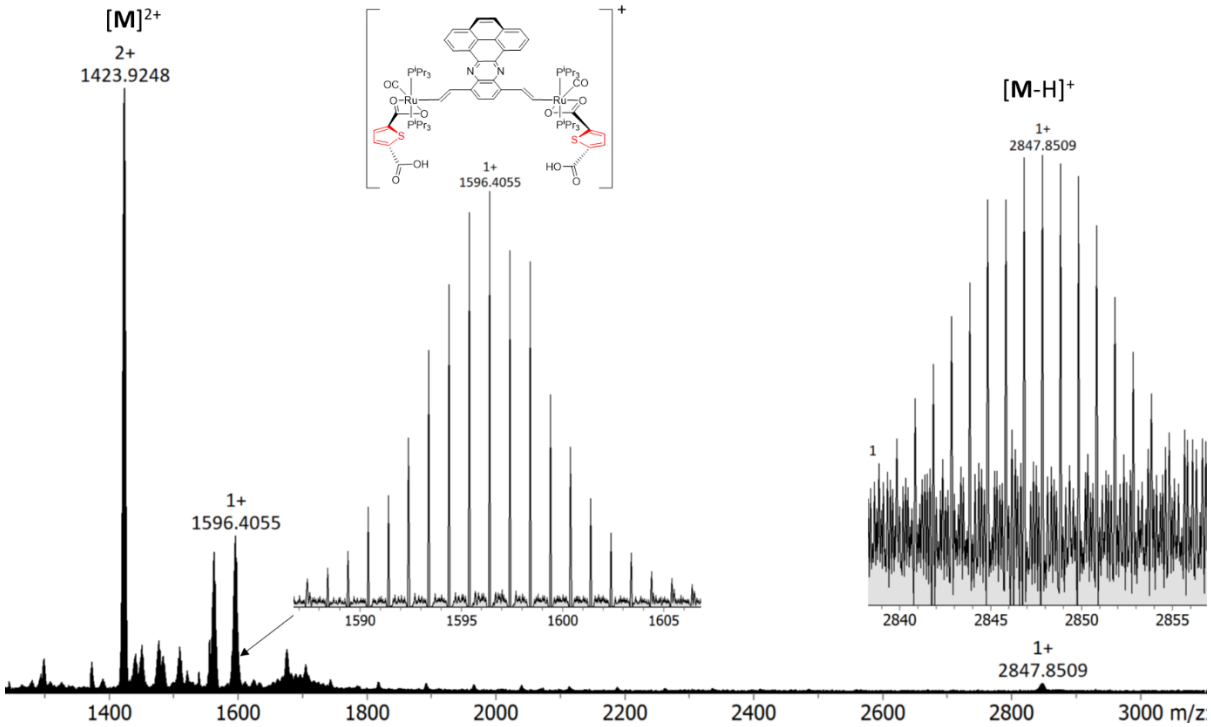

Figure S5. High-resolution electrospray ionisation mass spectrum (HR ESI-MS) of **Ru_4-5** (+ve ion mode).

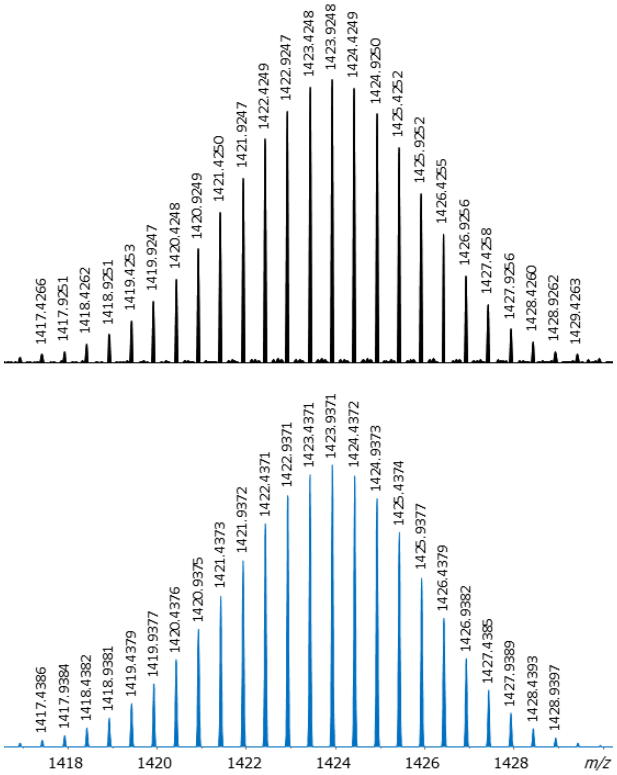

Figure S6. Isotopic pattern of the molecular ion $[M]^{2+}$ peak of **Ru_4-5**. Experimentally observed spectrum (black) is displayed on top and simulated spectrum (blue) is at the bottom.

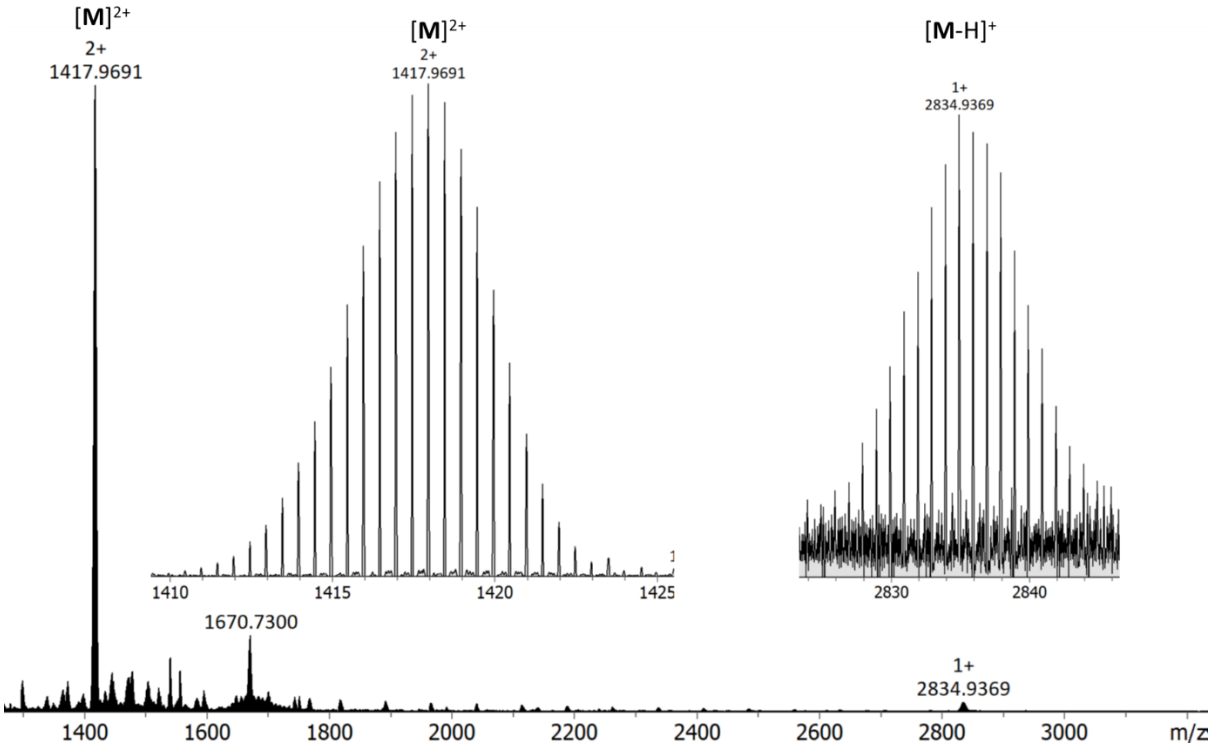

Figure S7. High-resolution electrospray ionisation mass spectrum (HR ESI-MS) of **Ru_4-6** (+ve ion mode).

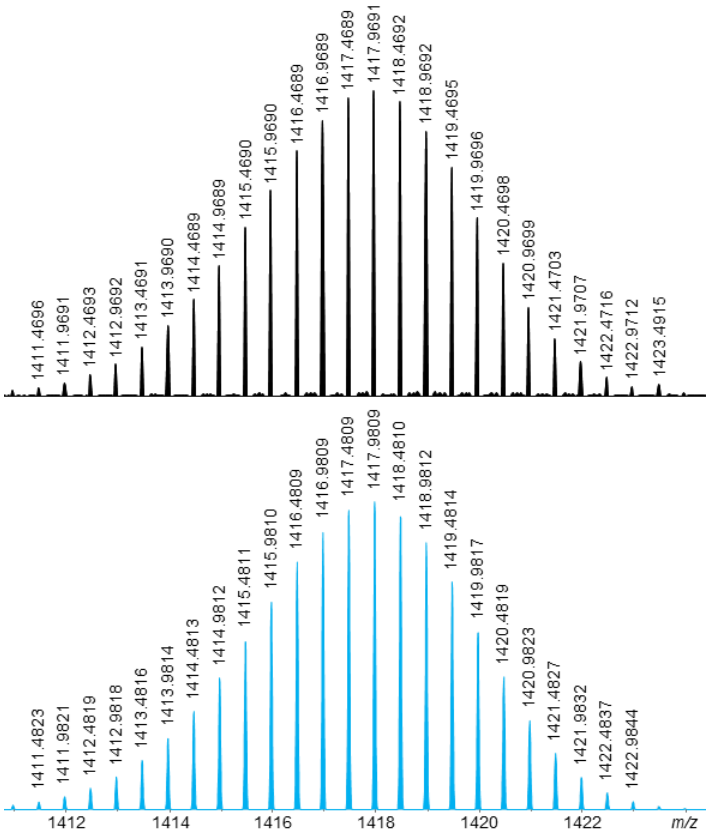

Figure S8. Isotopic pattern of the molecular ion $[\mathbf{M}]^{2+}$ peak of **Ru_4-6**. Experimentally observed spectrum (black) is displayed on top and simulated spectrum (blue) is at the bottom.

Table S1. Crystal data and structure refinement for **Ru_4-5**.

CCDC No.	2172028
Identification code	**Ru_4-5**
Empirical formula	$C_{72}H_{109}N_2O_8P_4Ru_2S$
Formula weight	1488.69
Temperature/K	100
Crystal system	monoclinic
Space group	$P2_1/c$
a/Å	14.8383(9)
b/Å	32.074(3)
c/Å	18.0081(12)
α/°	90
β/°	105.457(5)
γ/°	90
Volume/Å^3	8260.4(12)
Z	4
ρ_{calc}g/cm^3	1.197
μ/mm^{-1}	0.516
F(000)	3132.0
Crystal size/mm^3	0.4 × 0.203 × 0.01
Radiation	Mo Kα (λ = 0.71073)
2Θ range for data collection/°	3.416 to 44.032
Index ranges	$-15 \leq h \leq 15$, $-28 \leq k \leq 33$, $-17 \leq l \leq 18$
Reflections collected	21230
Independent reflections	21582 [R_{int} = 0.0656, R_{sigma} = 0.0770]
Data/restraints/parameters	21582/53/870
Goodness-of-fit on F^2	0.848
Final *R* indexes [I>=2σ (I)]	R_1 = 0.0764, wR_2 = 0.1935
Final *R* indexes [all data]	R_1 = 0.1249, wR_2 = 0.2390
Largest diff. peak/hole / e Å^{-3}	0.73/-0.67

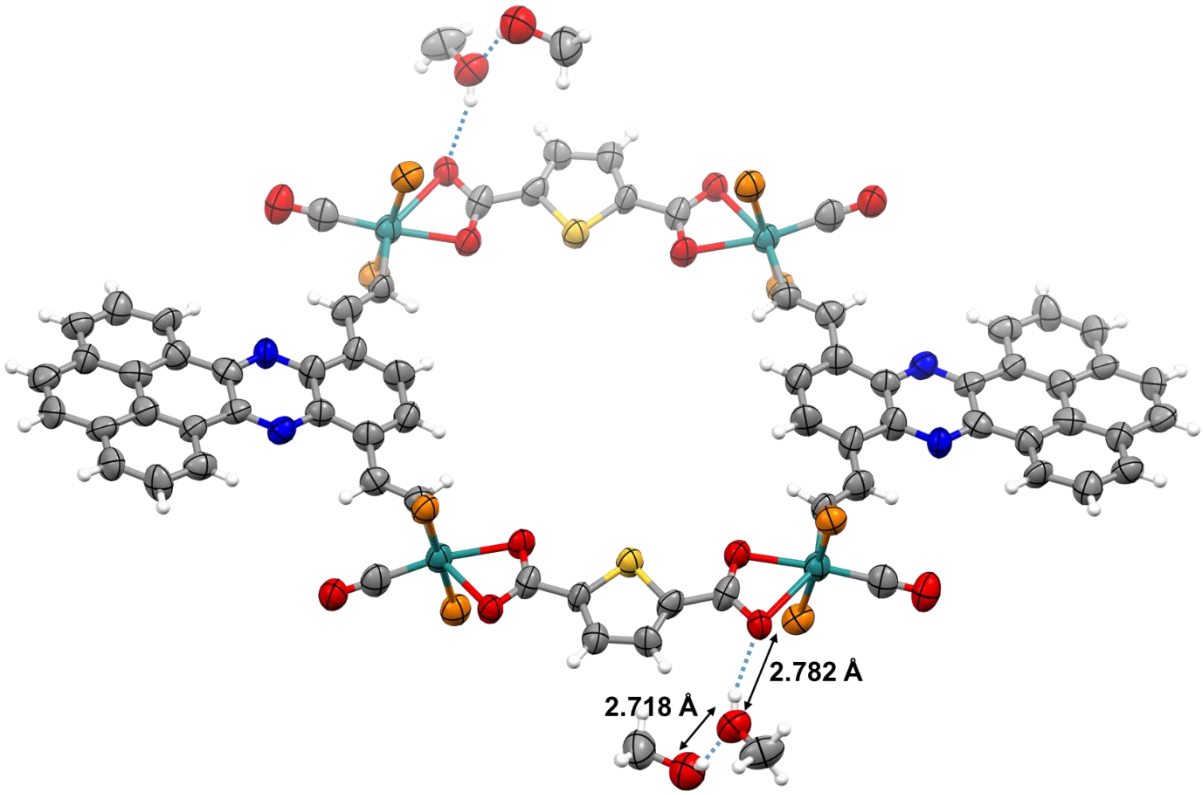

Figure S9. The intermolecular hydrogen bonding interactions with the co-crystallized solvent methanol molecules to one of the carboxylate functional groups of **Ru_4-5** is shown. The C atoms at the isopropyl groups of the P^iPr_3 ligands are removed for clarity reasons. The ellipsoids are displayed at a 50% probability level. Colour codes: grey, carbon; red, oxygen; orange, phosphorous; white, hydrogen; green, chlorine; and dark turquoise, ruthenium.

Cyclic voltammetry

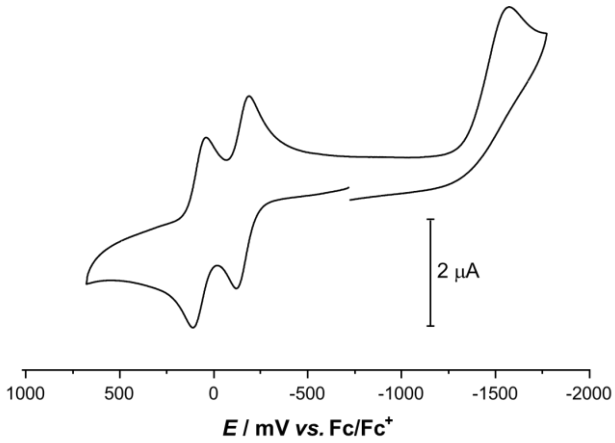

Figure S10. Cyclic voltammogram of **Ru_2-3** at v = 100 mV/s with 0.1 M $TBAPF_6$ supporting electrolyte in dichloromethane at 295(±3) K.

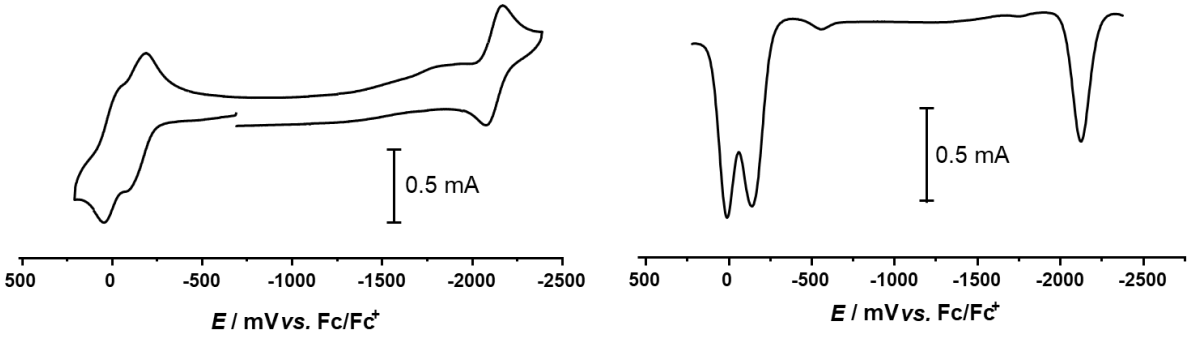

Figure S11. Cyclic (left) (v = 100 mV/s) and square-wave voltammograms (right) of **Ru_4-5** with 0.1 M $TBAPF_6$ supporting electrolyte in THF at 295(±3) K.

Table S2. Data of cyclic voltammetric measurements of tetraruthenium macrocycle **Ru_4-5** at different scan rates measured in THF/^{n}Bu_4NPF_6.

Scan rate v in mV/s	**$E_{1/2}^{0/2+}$ in mV**	**$\Delta E_p^{0/2+}$ in mV**	**$E_{1/2}^{2+/4+}$ in mV**	**$\Delta E_p^{2+/4+}$ in mV**	**$E_{1/2}^{0/2-}$ in mV**	**$\Delta E_p^{0/2-}$ in mV**
100	-134	101	-6	106	-2118	96.5
200	-137	102	-5	95	-2123	107
400	-139	105	0	79	-2119	108
600	-135	113	4	82	-2121	113
800	-140	111	5	79	-2121	125
1000	-140	110	3	87	-2124	129
1500	-141	117	3	93	-2124	141
2000	-135	128	7	94	-2124	149

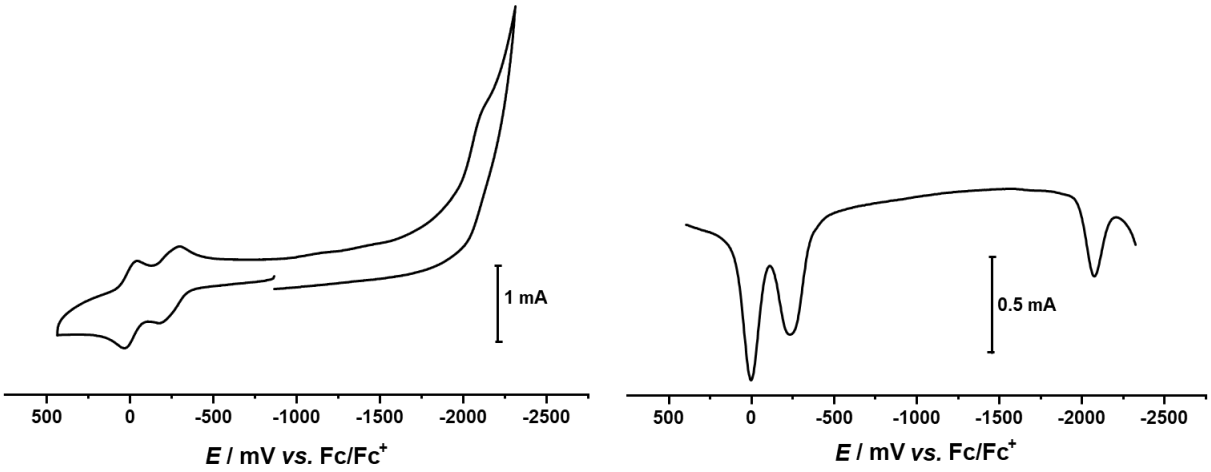

Figure S12. Cyclic (left) (v = 100 mV/s) and square-wave voltammograms (right) of **Ru_4-5** with 0.1 M $TBAPF_6$ supporting electrolyte in dichloromethane (DCM) at 295(±3) K.

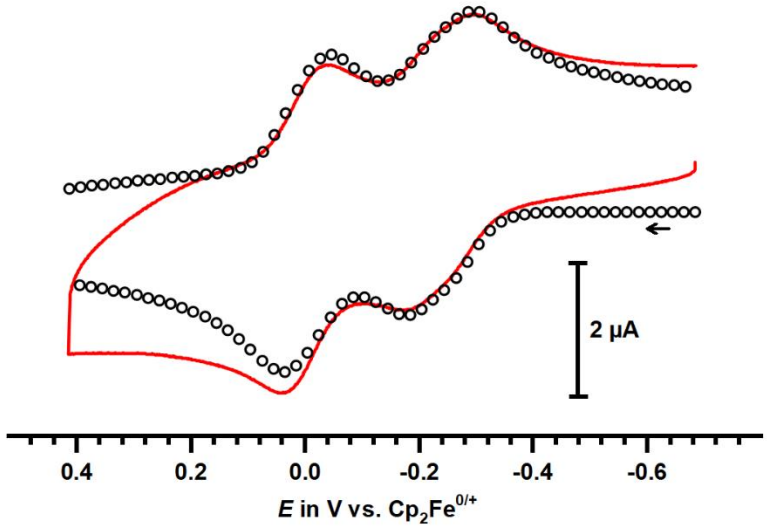

Figure S13. Simulated cyclic voltammogram (v = 400 mV/s) of the two oxidation waves of **Ru_4-5** with 0.1 M $TBAPF_6$ supporting electrolyte in dichloromethane (DCM) at 295(±3) K.

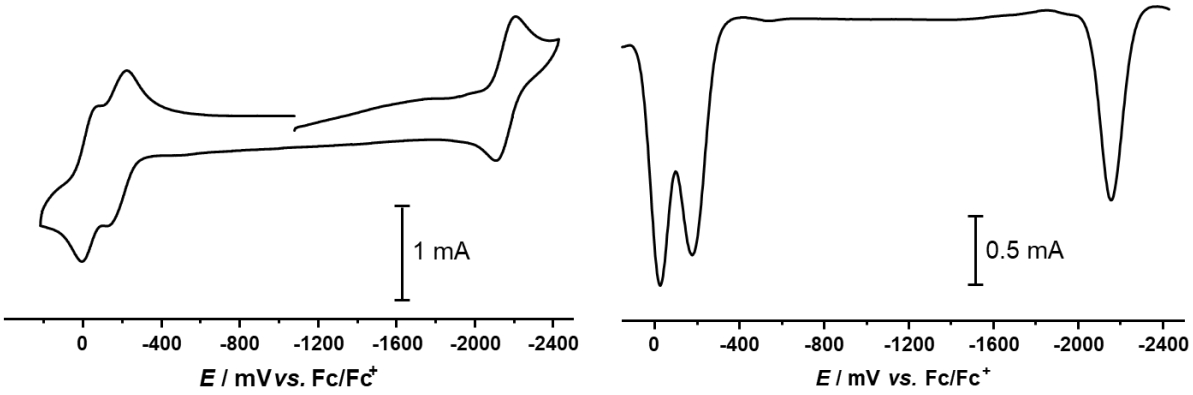

Figure S14. Cyclic (left) (v = 100 mV/s) and square-wave voltammograms (right) of **Ru_4-6** with 0.1 M $TBAPF_6$ supporting electrolyte in THF at 295(±3) K.

Table S3. Data of cyclic voltammetric measurements of tetraruthenium macrocycle **Ru_4-6** at different scan rates measured in THF/$^nBu_4NPF_6$.

Scan rate v in mV/s	**$E_{1/2}^{0/2+}$ in mV**	**$\Delta E_p^{0/2+}$ in mV**	**$E_{1/2}^{2+/4+}$ in mV**	**$\Delta E_p^{2+/4+}$ in mV**	**$E_{1/2}^{0/2-}$ in mV**	**$\Delta E_p^{0/2-}$ in mV**
25	-170	98	-29	75	-2151	97
50	-173	93	-30	73	-2150	92
100	-173	99	-32	77	-2148	103
200	-175	103	-32	83	-2151	111
400	-172	103	-30	84	-2155	110
600	-176	106	-40	89	-2152	117
800	-173	115	-35	85	-2151	126
1000	-174	112	-31	91	-2152	135
1500	-172	117	-29	100	-2154	139
2000	-172	124	-30	101	-2155	150

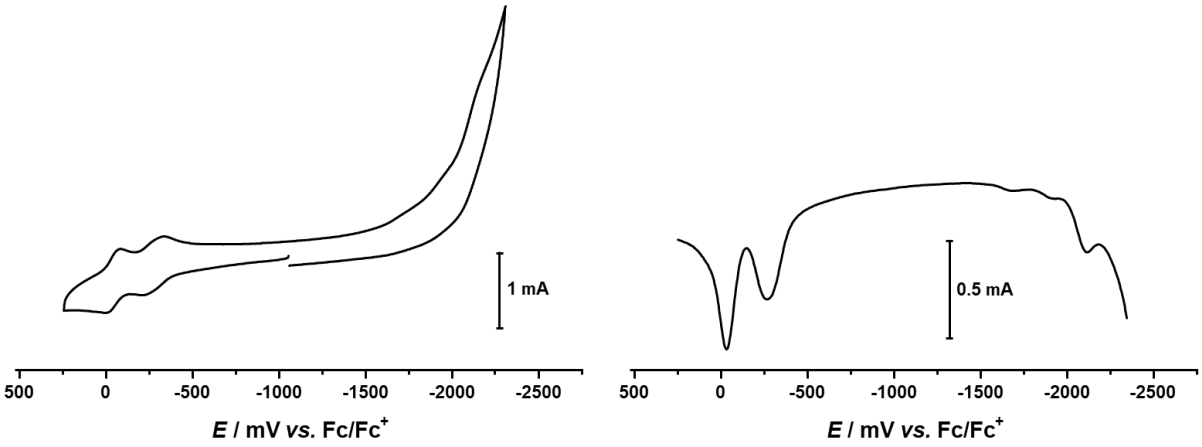

Figure S15. Cyclic (left) (v = 100 mV/s) and square-wave voltammograms (right) of **Ru_4-6** with 0.1 M $TBAPF_6$ supporting electrolyte in dichloromethane (DCM) at 295(±3) K.

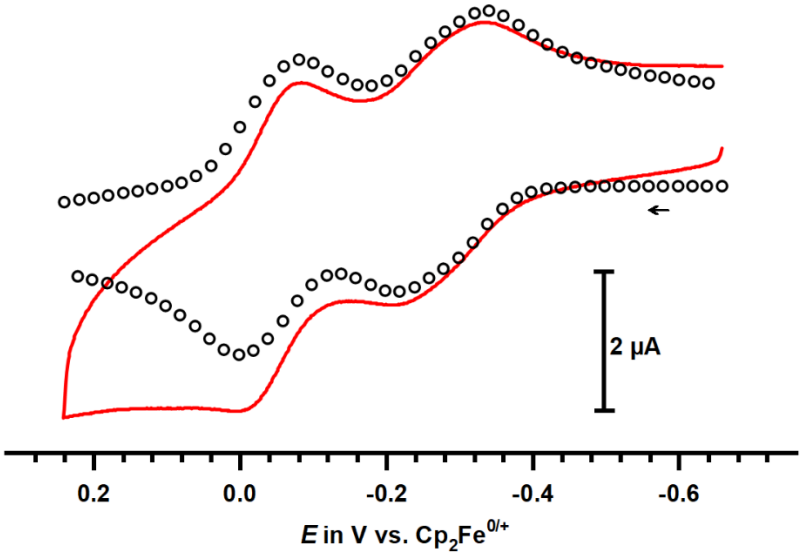

Figure S16. Simulated cyclic voltammogram (v = 100 mV/s) of the two oxidation waves of **Ru_4-6** with 0.1 M $TBAPF_6$ supporting electrolyte in dichloromethane (DCM) at 295(±3) K.

Spectra recorded from chemically or electrochemically oxidized compounds

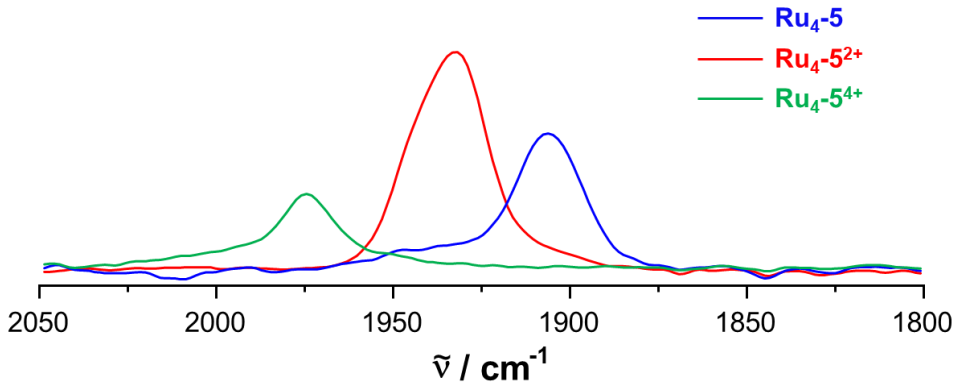

Figure S17. Changes in the mid-IR [Ru(CO)] spectra of **Ru₄-5** upon oxidation from **Ru₄-5** (blue) to [**Ru₄-5**]$^{2+}$ (red) and second oxidation from [**Ru₄-5**]$^{2+}$ to [**Ru₄-5**]$^{4+}$ (green) in dichloromethane at 298 K.

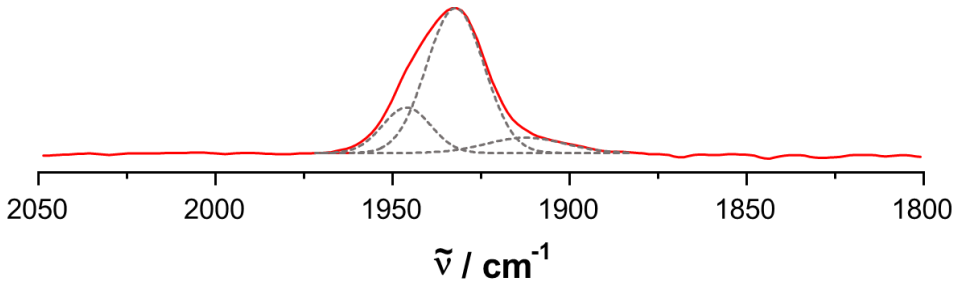

Figure S18. Deconvoluted [Ru(CO)] spectrum of [**Ru₄-5**]$^{2+}$. The red line represents the experimentally observed spectrum and dotted grey lines are individual contributions in the deconvoluted spectra.

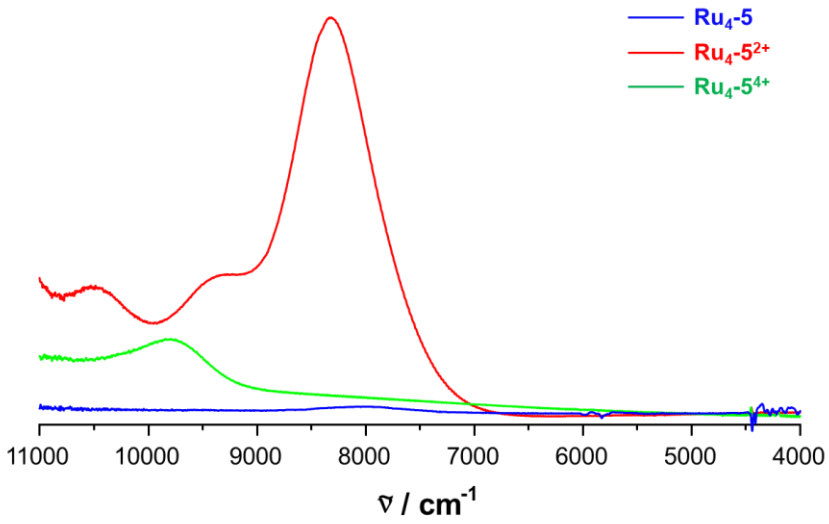

Figure S19. Spectroscopic changes in the NIR region upon oxidation of **Ru₄-5** (blue) to [**Ru₄-5**]$^{2+}$ (red) and further oxidation to [**Ru₄-5**]$^{4+}$ (green) in dichloromethane at 298 K.

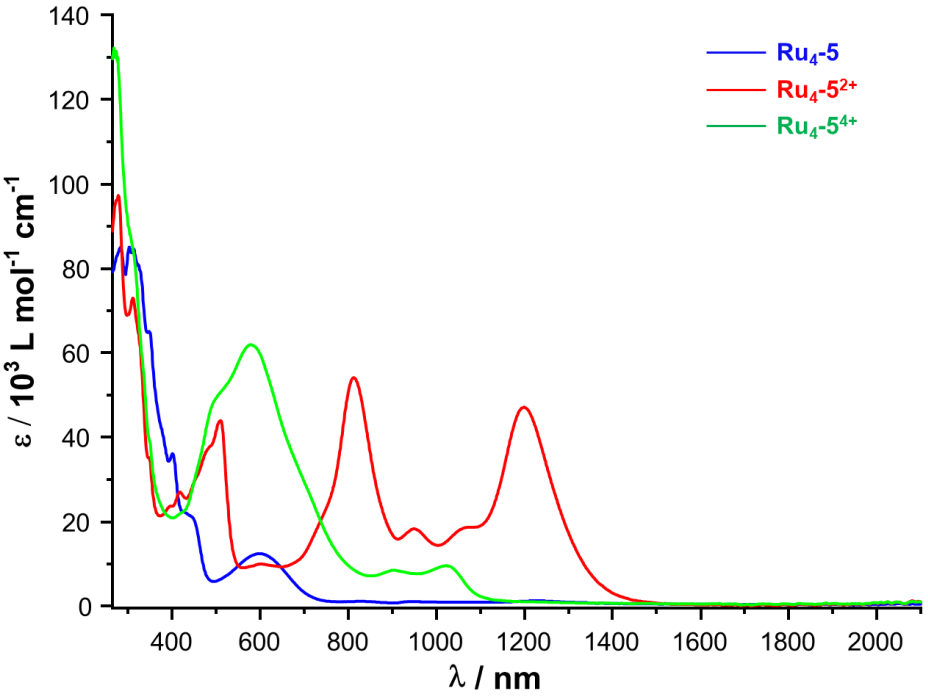

Figure S20. Spectroscopic changes in the UV/vis/NIR region upon oxidation of **Ru₄-5** (blue) to [**Ru₄-5**]$^{2+}$ (red) and further oxidation to [**Ru₄-5**]$^{4+}$ (green) in dichloromethane at 298 K.

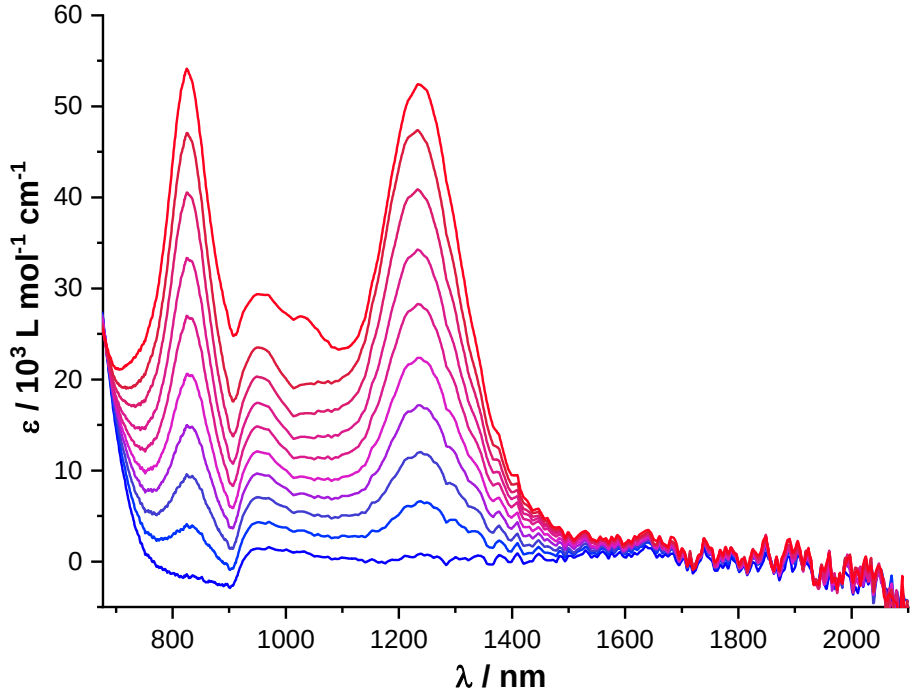

Figure S21. Spectroscopic changes in the UV/vis/NIR region upon oxidation of **Ru₄-5** (blue) to [**Ru₄-5**]$^{2+}$ (red) in dichloromethane at 298 K.

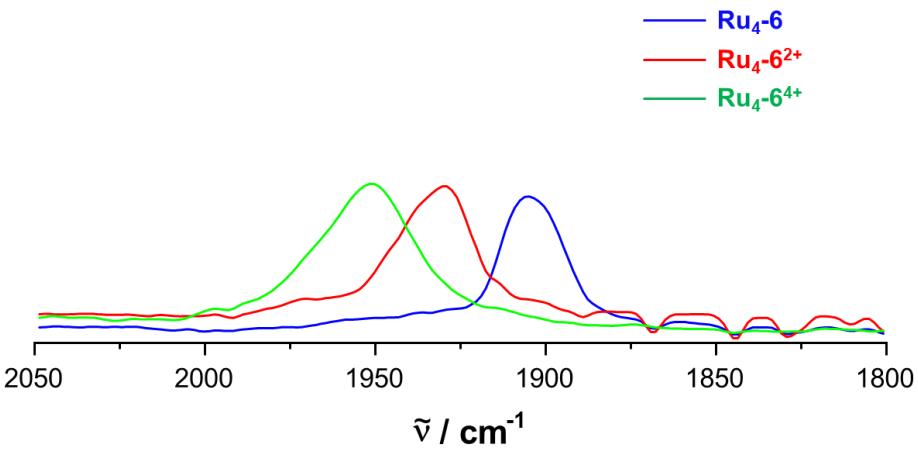

Figure S22. Changes in the mid-IR [Ru(CO)] spectra of **Ru$_4$-6** upon oxidation from **Ru$_4$-6** (blue) to [**Ru$_4$-6**]$^{2+}$ (red) and second oxidation from [**Ru$_4$-6**]$^{2+}$ to [**Ru$_4$-6**]$^{4+}$ (green) in dichloromethane at 298 K.

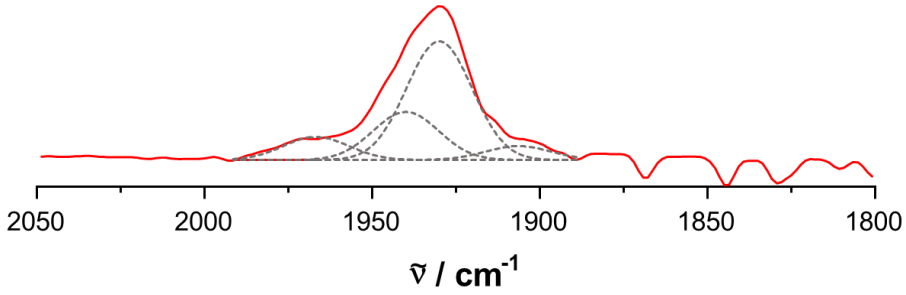

Figure S23. Deconvoluted [Ru(CO)] spectrum of [**Ru$_4$-6**]$^{2+}$. The red line represents the experimentally observed spectrum and dotted grey lines are the individual contributions to the deconvoluted spectra.

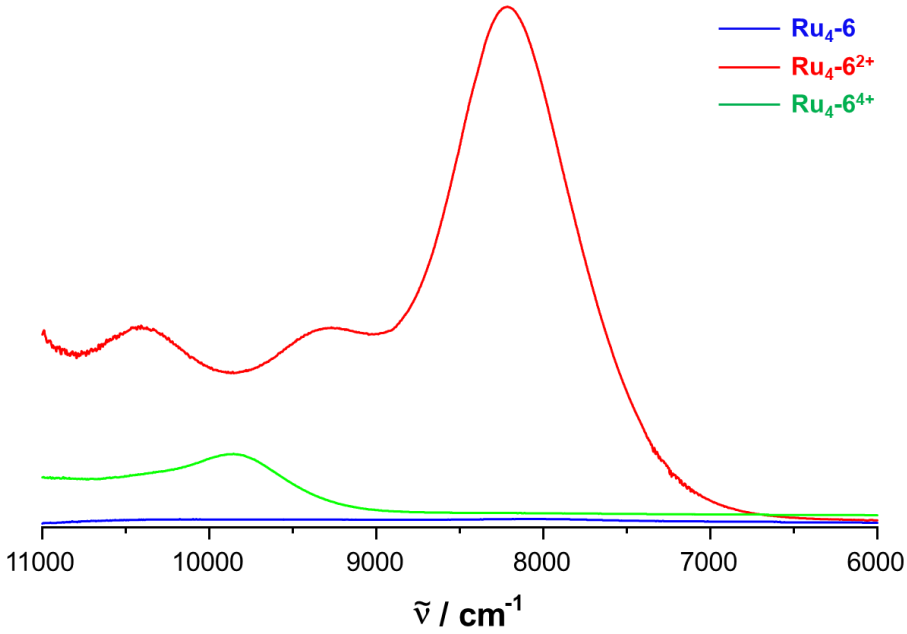

Figure S24. Spectroscopic changes in the NIR region upon oxidation of **Ru$_4$-6** (blue) to [**Ru$_4$-6**]$^{2+}$ (red) and further oxidation to [**Ru$_4$-6**]$^{4+}$ (green) in dichloromethane at 298 K.

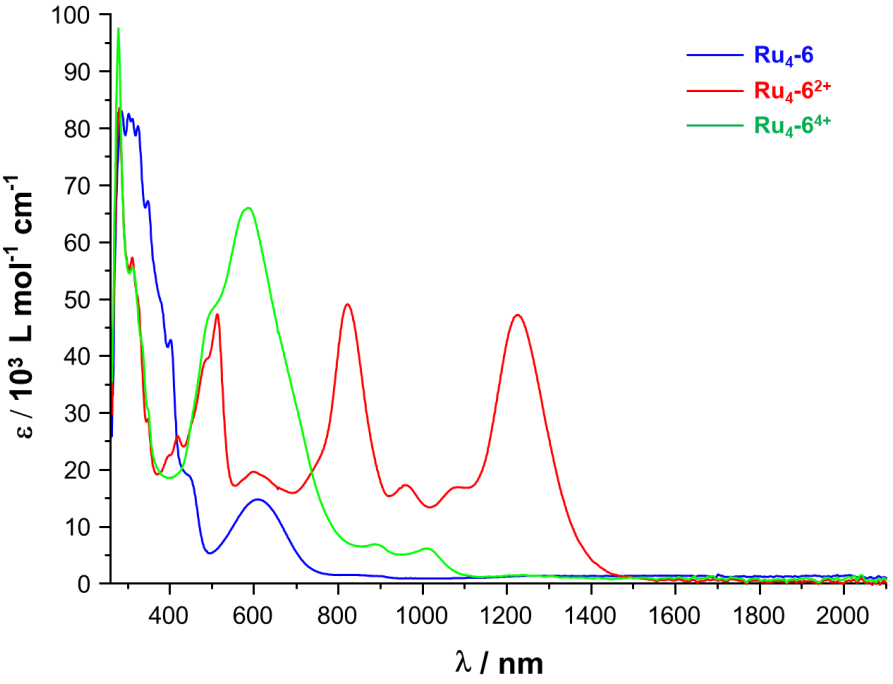

Figure S25. Spectroscopic changes in the UV/vis/NIR region upon oxidation of **Ru$_4$-6** (blue) to [**Ru$_4$-6**]$^{2+}$ (red) and further oxidation to [**Ru$_4$-6**]$^{4+}$ (green) in dichloromethane at 298 K.

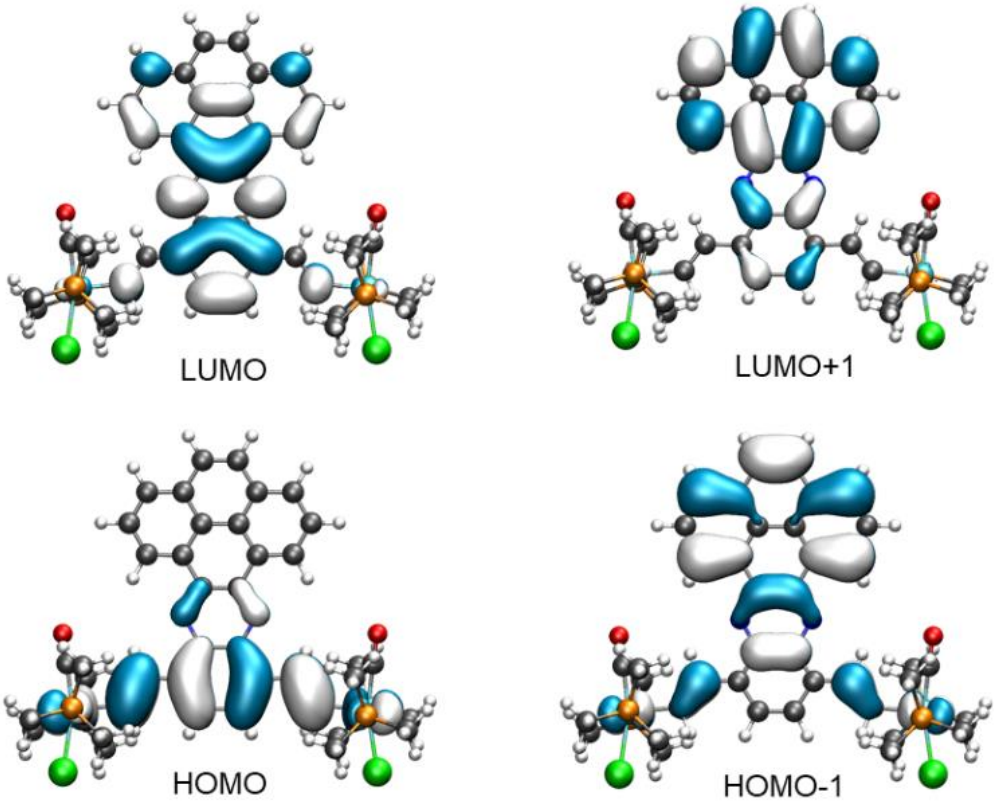

Figure S26. Contour plots of the calculated HOMO, HOMO-1, LUMO and LUMO+1 of model complex ^{Me}**Ru$_2$-3** (PBE1PBE/6-31G(d)PCM(CH_2Cl-CH_2Cl).

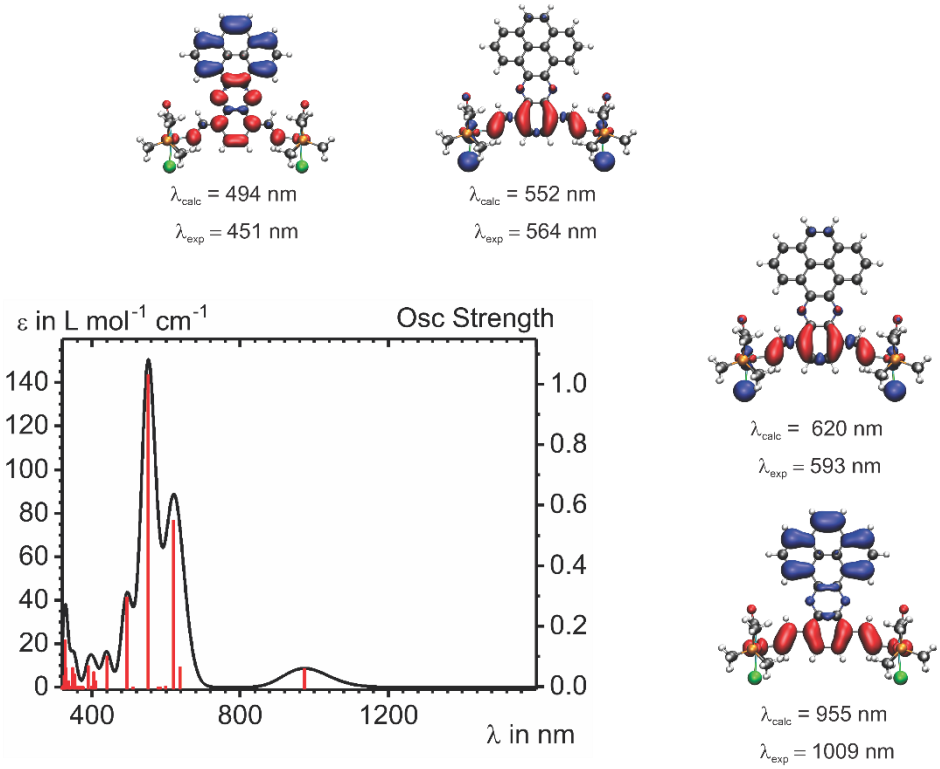

Figure S27. Calculated UV-vis-NIR spectrum of **[^{Me}Ru$_2$-3]$^{2+}$** in its electronic singlet state as obtained from the TD-DFT calculations. The red colour marks an increase, the blue colour a decrease of electron density during the corresponding electronic transition.

EPR Spectroscopy

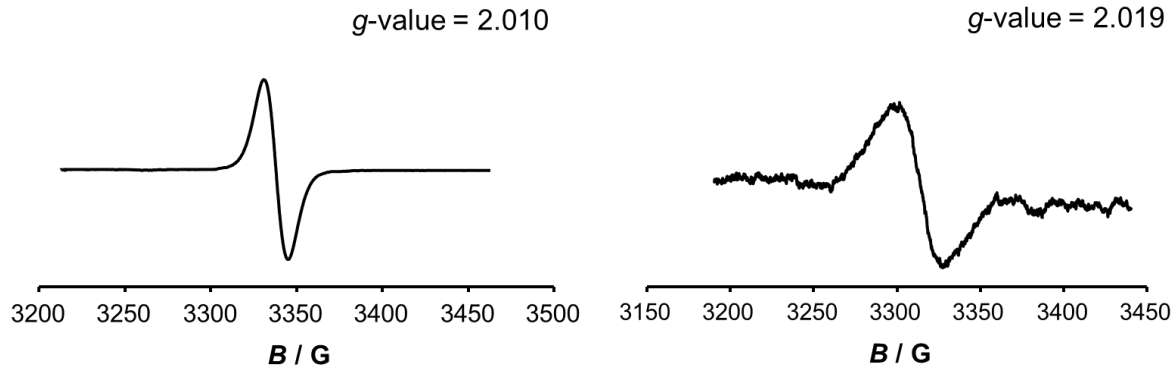

Figure S28. EPR Spectra of **[Ru$_4$-5]$^{2+}$** (left) and **[Ru$_4$-5]$^{4+}$** (right) measured at 298K.

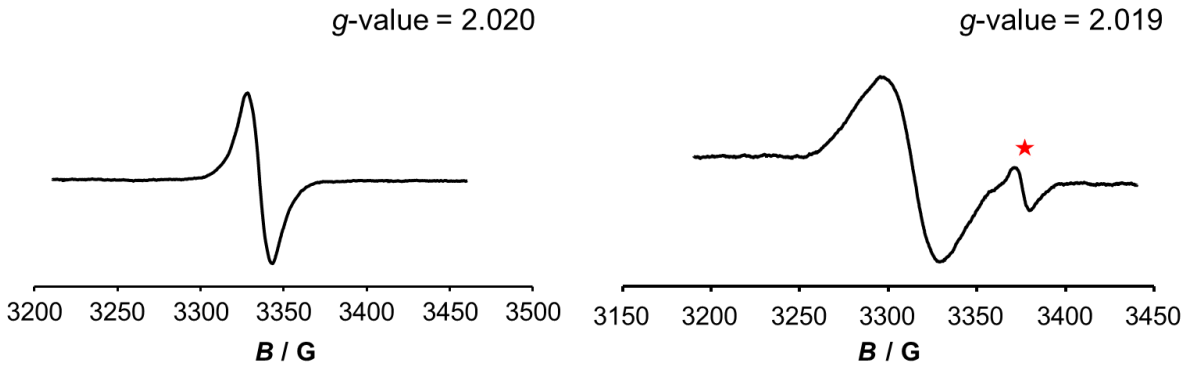

Figure S29. EPR Spectra of **[Ru$_4$-6]$^{2+}$** (left) and **[Ru$_4$-6]$^{4+}$** (right) measured at 298K.

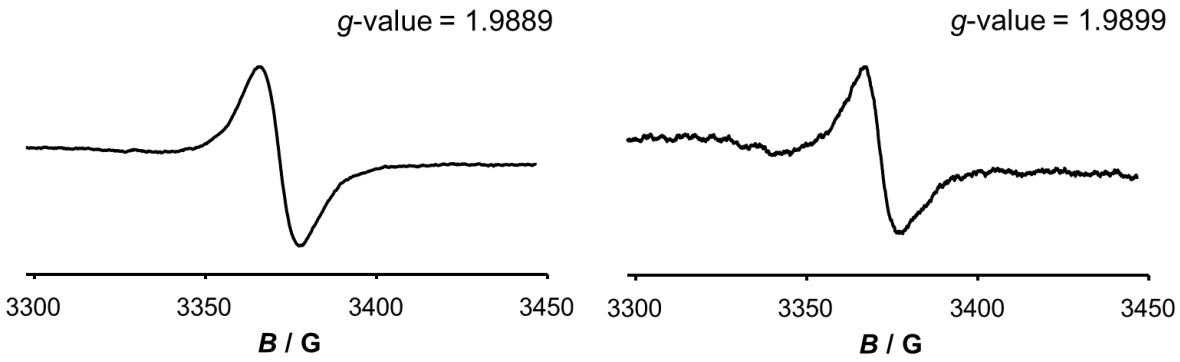

Figure S30. EPR Spectra of reduced **[Ru$_4$-5]$^{2-}$** (left) and **[Ru$_4$-6]$^{2-}$** (right) measured at 298K.

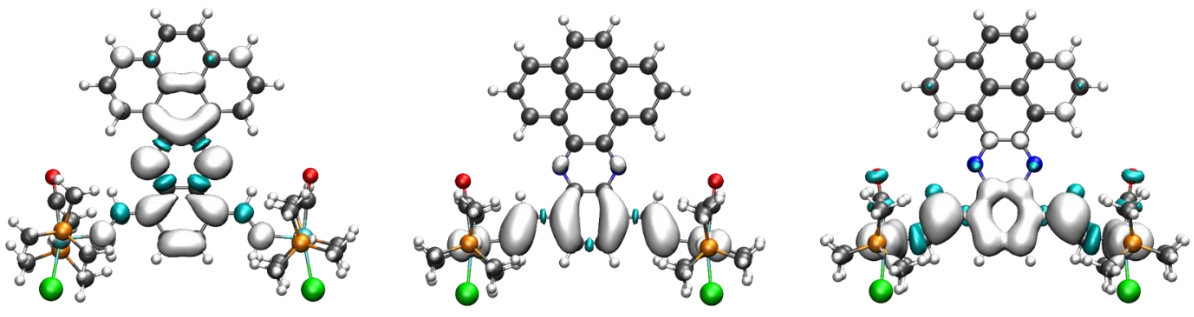

[Ru$_2$-3]$^-$ **[Ru$_2$-3]$^+$** **[Ru$_2$-3]$^{2+}$**

Figure S31. Computed spin densities for the radical anion (left), cation (middle) and the dication (right, triplet sate) of the model for complex **Ru_2-3**.

Synthesis and characterization of charge-transfer salts

Dichloromethane solutions of complexes **Ru_4-5**, **Ru_4-6** and F_4TCNQ were prepared in separate flasks. Then, for the synthesis of the CT salts, one equivalent of complex and two equivalents of F_4TCNQ were mixed. Immediate changes of colours from leafy-green to pale yellow-green (for **$[Ru_4\text{-}5]^{2+}$ $[F_4TCNQ^-]_2$, CT-1**) and dark green to yellow-green (for **$[Ru_4\text{-}6]^{2+}$ $[F_4TCNQ^-]_2$, CT-2**) were observed. Both the charge-transfer salts were characterized by EPR, IR and UV-vis-NIR spectroscopy.

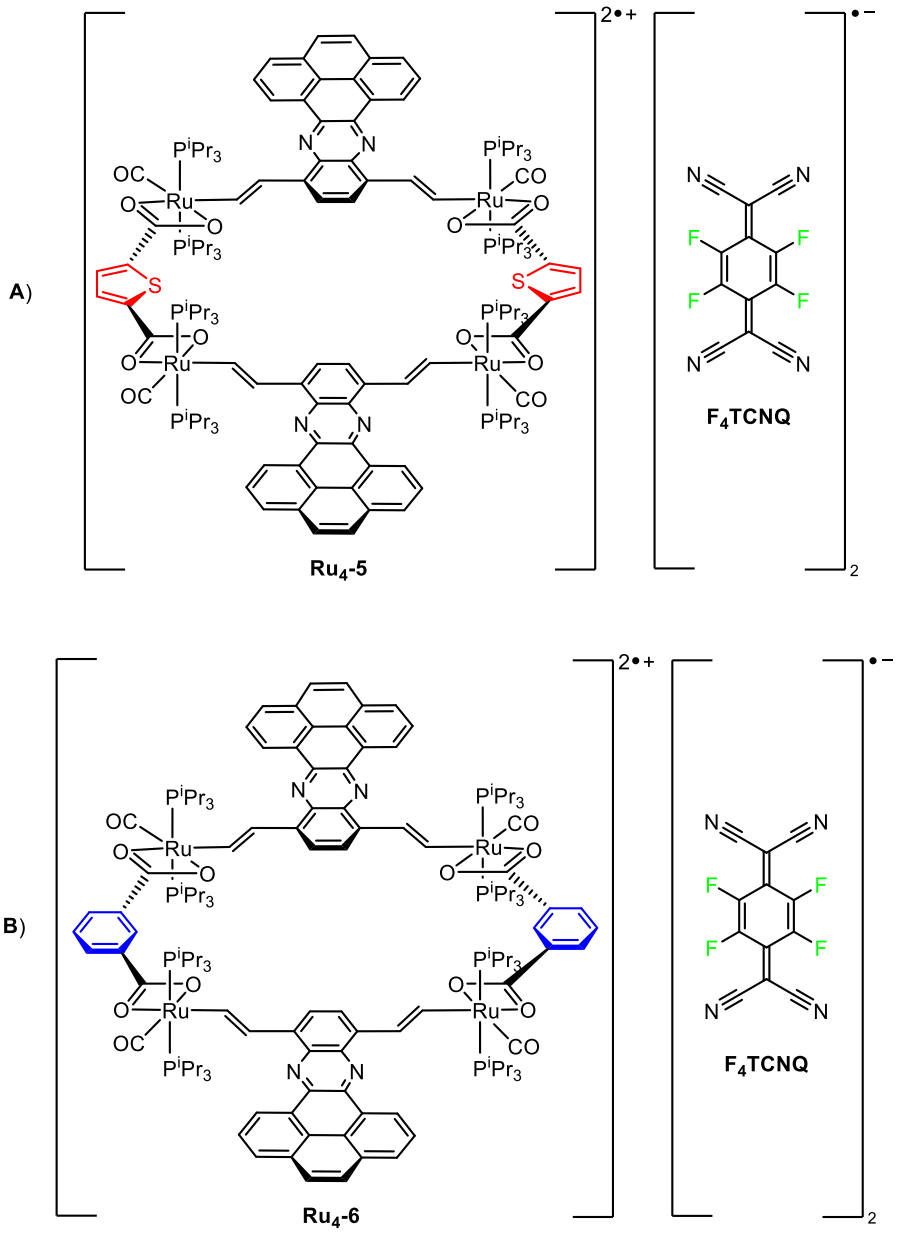

Figure S32. Charge-transfer salts **CT-1** (**A**) and **CT-2** (**B**) synthesized for this study.

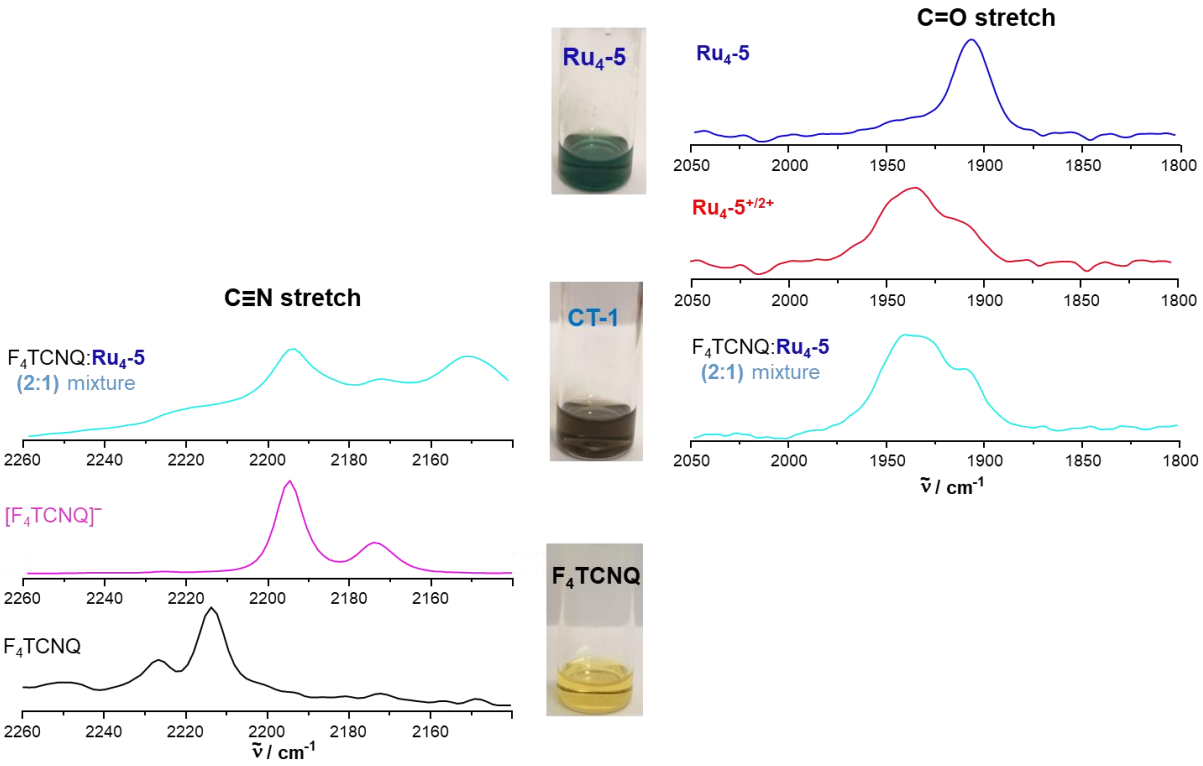

Figure S33. Monitoring the formation of salt **CT-1** (**1:2** mixture of **Ru₄-5** and F_4TCNQ) through IR spectroscopy.

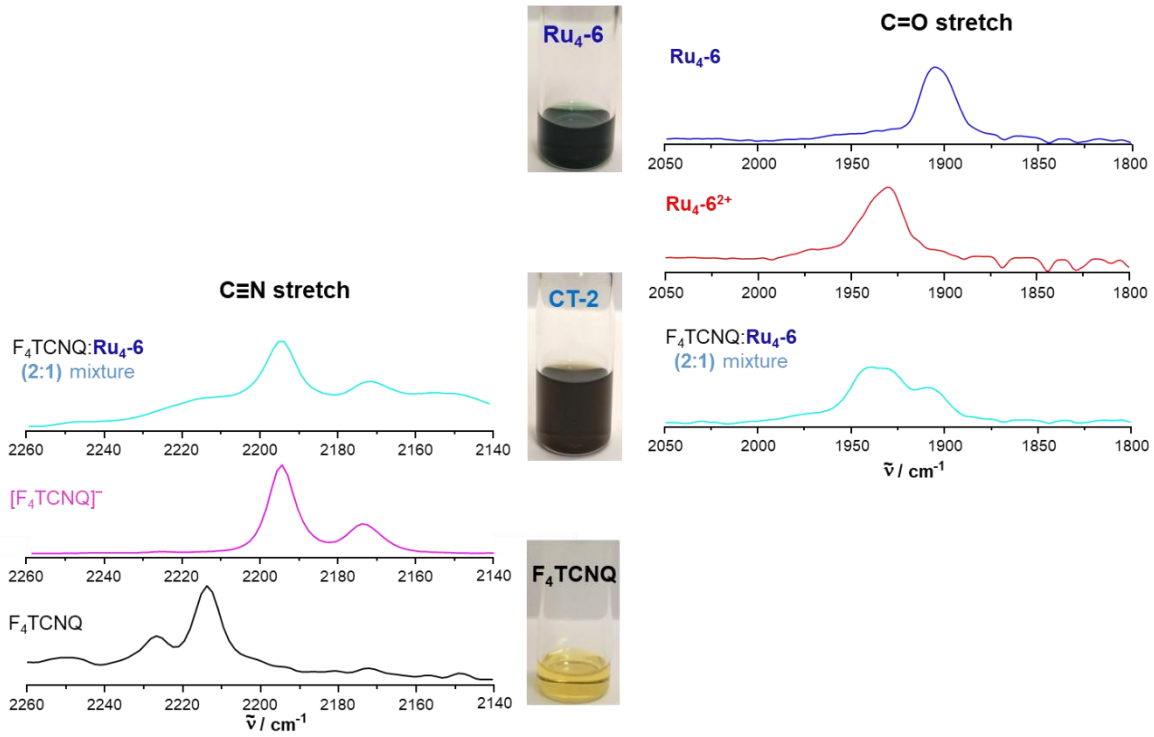

Figure S34. Monitoring the formation of salt **CT-2** (**1:2** mixture of **Ru₄-6** and F_4TCNQ) through IR spectroscopy.

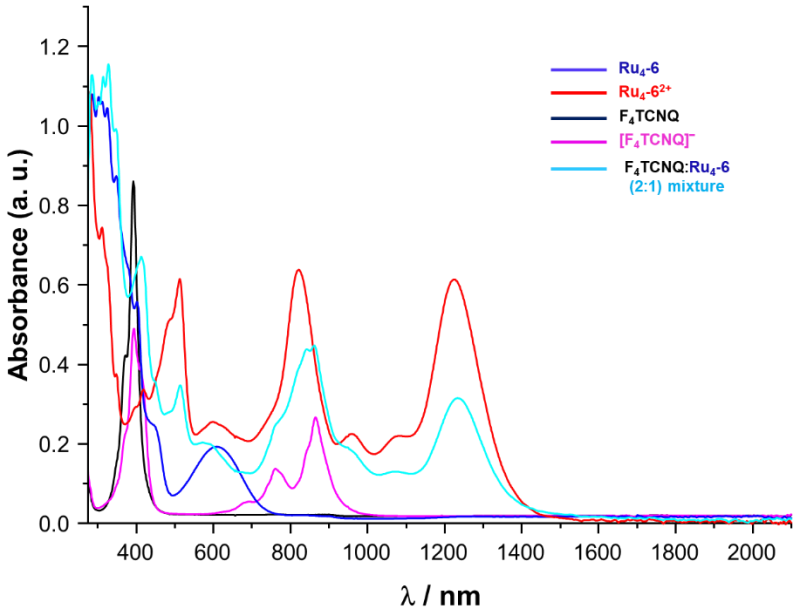

Figure S35. The UV/vis/NIR spectrum of **CT-2** salt (1:2 mixture of **Ru$_4$-6** and F_4TCNQ) is plotted with those of the neutral complex, neutral F_4TCNQ, oxidized complex **[Ru$_4$-6]**$^{2+}$ and mono-reduced F_4TCNQ for comparison purposes.

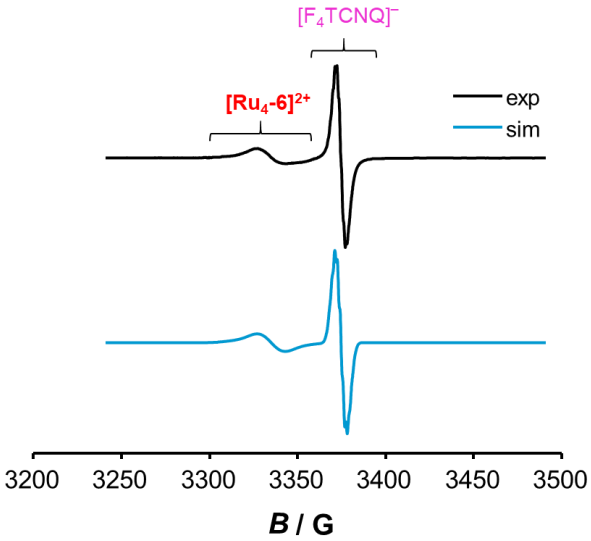

Figure S36. EPR spectrum of salt **CT-2**. Separate resonance signals for the radical cation and radical anion are clearly observed. The experimental spectrum is shown at the top and simulated one is at the bottom; *g*-values of 2.0240 and 1.9876 were obtained for **[Ru$_4$-5]**$^{2+}$ and $[F_4TCNQ]^-$, respectively.

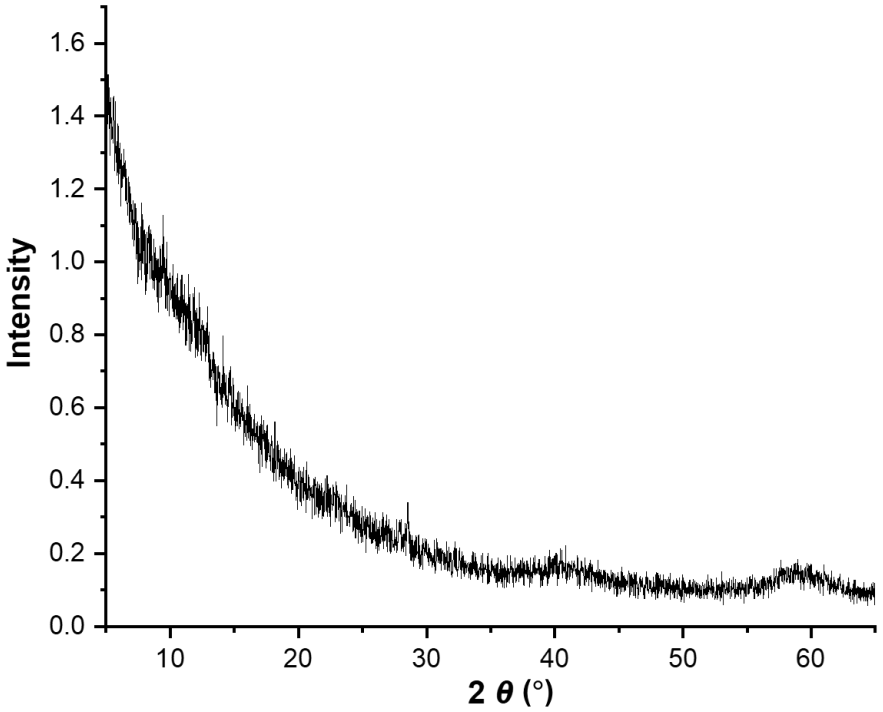

Figure S37. Powder X-ray diffraction (PXRD) pattern of the charge-transfer salt **CT-1** (**[Ru$_4$-5]**$^{2+}$ [F_4TCNQ]$_2^-$).

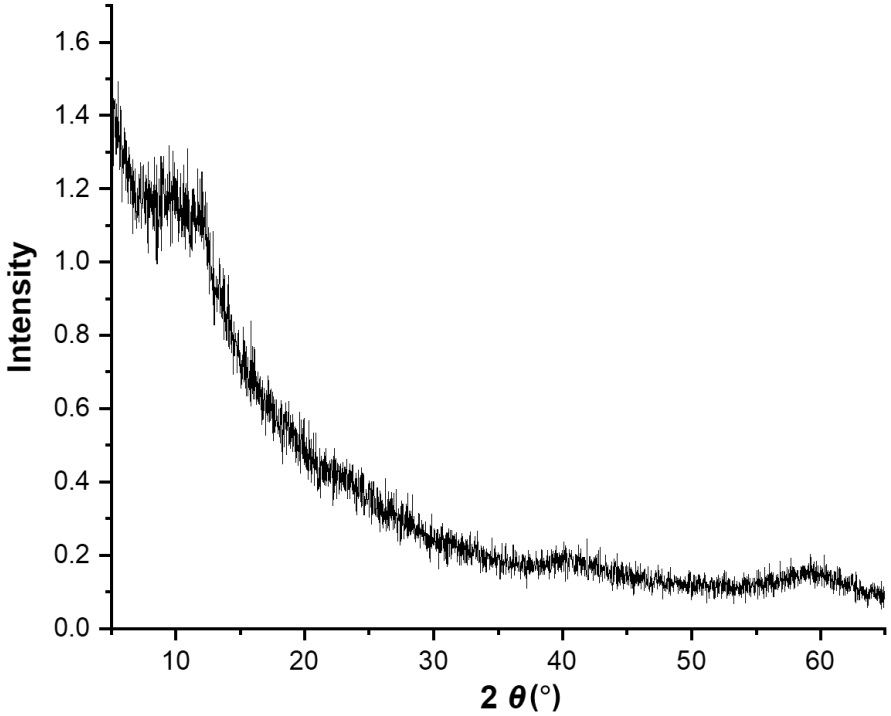

Figure S38. Powder X-ray diffraction (PXRD) pattern of the charge-transfer salt **CT-2** (**[Ru$_4$-6]**$^{2+}$ [F_4TCNQ]$_2^-$).